

## Modelling of non-steady-state transition from single-point to two-point rolling contact

Yang, Zhen; Li, Zili; Dollevoet, Rolf

**DOI**

[10.1016/j.triboint.2016.04.023](https://doi.org/10.1016/j.triboint.2016.04.023)

**Publication date**

2016

**Document Version**

Accepted author manuscript

**Published in**

Tribology International

**Citation (APA)**

Yang, Z., Li, Z., & Dollevoet, R. (2016). Modelling of non-steady-state transition from single-point to two-point rolling contact. *Tribology International*, 101(September), 152-163.  
<https://doi.org/10.1016/j.triboint.2016.04.023>

**Important note**

To cite this publication, please use the final published version (if applicable).  
Please check the document version above.

**Copyright**

Other than for strictly personal use, it is not permitted to download, forward or distribute the text or part of it, without the consent of the author(s) and/or copyright holder(s), unless the work is under an open content license such as Creative Commons.

**Takedown policy**

Please contact us and provide details if you believe this document breaches copyrights.  
We will remove access to the work immediately and investigate your claim.

# Modelling of non-steady-state transition from single-point to two-point rolling contact

Zhen Yang, Zili Li and Rolf Dollevoet

Section of Road and Railway Engineering, Faculty of Civil Engineering and Geosciences, Delft University of Technology, Stevinweg 1, 2628 CN Delft, the Netherlands

## ABSTRACT

By considering real wheel and track geometry and structures, as well as their coupled interaction, an explicit finite element method is applied to simulate the transition of wheel-rail rolling from single-point tread contact to two-point tread-flange contact. The evolutions of the contact position, stress magnitude and direction, adhesion-slip distribution, and wheel-rail relative velocities in the two contact patches are considered to investigate the transient dynamic effects during the contact transition. Important findings include that the transition to two-point contact can result in friction saturation and excite waves in the contact, causing local intensification and relaxation of compression, as well as turbulence of the micro-slip; the local relative velocity in the contact patch is a good measure of the dynamic effects.

Keywords: frictional rolling, wheel-rail contact, two-point contact, non-steady state

## 1. INTRODUCTION

Wheel/rail rolling contact is more complex on curves than on straight tracks. Because the leading wheelset often fails to align itself tangentially with the rails, an angle of attack (AoA) arises, and non-Hertzian two-point contact may occur on the high rail: the wheel tread contacts the rail top surface at the same time that the wheel flange contacts the rail gauge corner.

Complex two-point contact is difficult to model, as it involves arbitrary wheel and rail geometries, large creepage and spin. Traditional approaches based on the half-space assumption, such as Hertz's analytical method, virtual-penetration-based methods [1,2], and Kalker's program FASTSIM and CONTACT [3], are considered inaccurate because the radii of curvature of the contact bodies at the flange-gauge corner contact can be of the same size as the contact patch and the patch may be non-planar. ANALYN [4] and FaStrip [5], though also limited to the half-space assumption, were proposed as alternatives to the virtual-penetration-based methods and FASTSIM, with higher accuracies in terms of both creep force estimation and shear stress distribution, especially when the contact patch is non-elliptic. By extending the CONTACT algorithm to quasi-quarter-spaces, Li [6] presented the program WEAR to cope with conformal contact, including two-point contact. Its application to contact between a wheel and the switch blade of a turnout is presented in [7].

As CONTACT and WEAR are based on the boundary element method [6], they can only treat linear-elastic materials and idealized contact geometry, limiting their accuracy in analyses of wear and rolling contact fatigue (RCF) with large plastic deformation and arbitrary

contact geometry. The use of the finite element method (FEM) was proposed to overcome these problems. The elastic half-space contact solutions calculated by the FEM correspond well with those obtained from Hertz contact theory [8]. The FEM was also proven to be applicable to two-point wheel-rail contact, as satisfying solutions have been obtained for contact points on the rail top and gauge corner [9-12]. A good integration between 3D FEM and multibody modelling is archived in [13] to have a full description of vehicle dynamics.

The models in [8-13] all assumed quasi-static state contact between the discretised wheel and rail models. However, dynamic effects may play significant roles under certain circumstances, such as impact contact at geometric irregularities of the wheel and rail surfaces. To consider such dynamic effects, the explicit FEM was adopted to simulate the fatigue and wear of the rail joint [14], the growth of squat [15] and damage to the crossing nose [16,17]. The transient elastic-plastic stress-strain states in the contact were calculated by employing elastoplastic materials in the models. By accounting for the normal load and creep force as well as a realistic contact geometry, the transient explicit FEM has been proven to be effective and accurate for solving single-point frictional rolling contact between the wheel tread and rail with small [18] or large spin [19] by comparing its quasi-static state solutions with those of Hertz and CONTACT. In comparison with the implicit FEM, the explicit integration scheme avoids the regularization of the friction law [20] required to treat the no-slip condition in the adhesion area and the convergence difficulties caused by the demanding contact conditions [21]. Moreover, the computation efficiency is considerably improved when considering high-frequency vibrations.

In addition to impact, dynamic effects may also need to be considered when unstable vibration of the wheel (e.g., during curve negotiation) is present. In such a situation, increased wear, RCF and corrugation are expected [22], and a squeal noise may occur [23]. The occurrence of unstable wheel vibration can be significantly influenced by the transition from single-point to two-point contact during wheel curving through curved tracks.

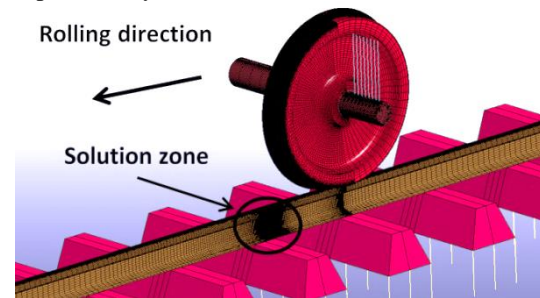
The explicit FEM has been applied to the analysis of wear and RCF in wheel curving with two-point contact [24]. The effects of the AoA were considered, and the contact positions with certain AoAs and wheel/rail profiles could be determined. Another application of the explicit FEM to two-point contact was presented in [25] to simulate the wear process on a laboratory twin-disc rig; good agreement was achieved by comparing the simulation results with the experimental results. However, in both cases, no dynamic effects were considered in the simulations, as the wheel motion was considered to be in the steady state and no unstable vibration occurred.

In this paper, the transition from single-point to two-point rolling contact is studied by employing an explicit FEM. The transition is a non-steady state process and occurs in a short period of time. The appearance of the second contact point may cause sudden changes in the normal and tangential forces at the two contact patches, exciting waves and friction-induced unstable vibrations. First, a FE model is presented to reproduce such a transient dynamic process numerically. Then, the contact solutions are carefully examined in terms of the evolutions of the contact position, the stress magnitude and direction, the adhesion-slip distribution, and the wheel-rail relative velocities in the two contact patches. The analyses show that waves are indeed excited in the contact patches when two-point contact occurs; to the authors' knowledge, this conclusion has not been previously revealed by either quasi-static or dynamic wheel-rail contact solutions. The ability to analyse the generation and propagation of the waves in rolling contact will enable a better understanding of dynamic rolling and its resulting wear (including fretting [26]) and RCF and may provide a basis for the study of the 'elusive' short-pitch corrugation and 'erratic' squeal noise, both of which are consequences of frictional contact.

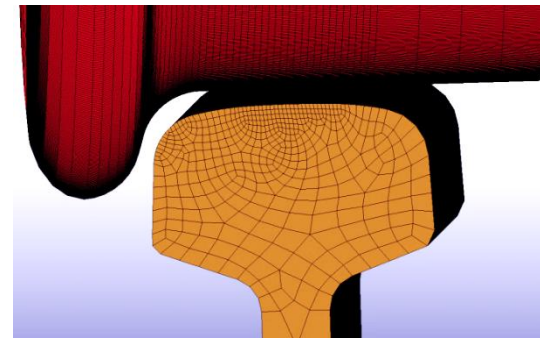
## 2. MODELLING AND VALIDATION OF THE WHEEL MODES

As shown in Fig. 1 (a), a 3D FE transient wheel-track interaction model is developed in which a 10 m length of half-track and a half-wheelset with the sprung mass of the car body and bogie are considered. The wheel, rail and sleepers are modelled using 8-node solid elements. To achieve a highly accurate solution with a reasonable model size, regular discretization is allocated at the wheel-rail contact areas and non-uniform meshing is used. The mesh size around the initial position of the wheel-rail contact and the 150-

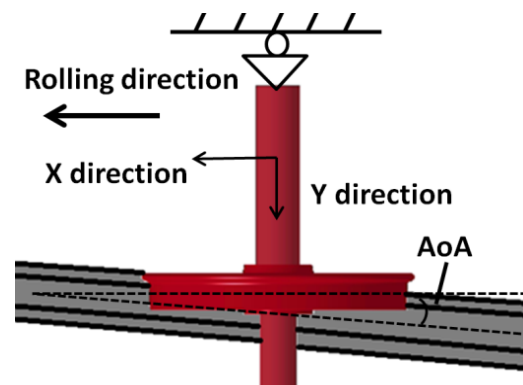
mm length of the solution zone is 1 mm. The lumped mass of the car body and bogie are modelled as mass elements connected to the wheelset by the primary suspension of the vehicle with parallel linear springs and viscous dampers. Each sleeper contains 12 solid elements, and the ballast is simplified as vertical spring and damper elements, with the displacements constrained in the lateral and longitudinal directions. The parameters involved in the track model are mainly taken from [27]. The wheel-rail contact is defined with real geometry, including the wheel flange and rail gauge corner, as shown in Fig. 1 (b), enabling the creepage and spin motion caused by the flange rubbing to be fully considered. The wheel geometry corresponds to a passenger car wheel of the Dutch railway with the standard profile of S1002; the rail is UIC54E1 with an inclination of 1:40. No geometry irregularities are considered on the surfaces of the wheel and rail. The friction coefficient is set to 0.6 to represent dry friction.



(a) Full FE model



(b) Wheel-rail profile/interaction



(c) Boundary condition

Fig. 1. Wheel-rail interaction model

The non-steady-state transition from single-point to two-point contact is simulated by applying the boundary condition to the wheel in the manner shown

in Fig. 1 (c). The lateral displacement is constrained at the inner side of the wheel axle, and the outer end of the axle is free. In the transient dynamic simulation, the wheel rolls from its initial position to the solution zone with an initial speed of 80 km/h along the X direction, forming an AoA with respect to the rail longitudinal direction. It is driven by a torque applied on the axle, thus generating a longitudinal creep force between the wheel and rail, which satisfies the requirement that the traction coefficient be below the friction coefficient. The wheel rolls with single-point contact between the wheel tread and rail crown before entering the solution zone. The damping in the system dissipates the initial kinetic and potential energy originating from any initial in-equilibrium of the system such that the system reaches a quasi-steady state upon arriving at the solution zone. Starting from this state, the wheel-rail rolling enters into the transition from single-point to two-point contact. This transient evolution will be captured and analysed in the solution zone.

The integration is performed in the time domain with an explicit central difference scheme. A small time step (86 ns) is employed for the model to meet the Courant stability condition [28]. This, together with the detailed modelling of the structure and continuum of the wheel/track system, guarantees that high-frequency dynamic effects up to 10 kHz are reproduced. The computation is carried out on a desktop workstation equipped with two Intel Xeon E5-2687 processors (8 cores in each processor) and 8\*8 GB RAM. 9 cores are employed in the computation and the memory consumption is around 3.2 GB. The total amounts of the nodes and elements processed are 651097 and 564786, respectively. The simulation is defined to run 0.67 m in about 349,000 time steps so that the contact patch moves approximately 1.93  $\mu\text{m}$  forward with each time step. This simulation took 28922 s (about 8 hours) to complete. In order to save the storage room of hard disc, an output time step 30  $\mu\text{s}$ , much larger than the computational time step of 86 ns, is adopted, during which the contact patch moves about 0.67 mm forward. The time steps mentioned below all refer to the output time step.

It is commonly believed that the dynamic effects during wheel curving are mainly generated by the vibration of the wheel [23]. The dynamics of the FE wheel model are thus validated here. All physical modes of the wheel are identified with an FE modal analysis within the frequency range of interest (10 kHz). For this, the same half-wheelset model as the explicit FE model is used, with the inner edge of its hub clamped. The calculated wheel modes under such a boundary condition can adequately represent the wheel dynamics under contact with the rail [29]. The identified frequencies of the axial, radial and circumferential modes are plotted in Fig. 2. Good agreement is observed when comparing the calculated results with the experimental wheel modal frequencies from [23], in which an NS-intercity wheel is measured for up to 5 kHz. All of these physical modes can be naturally included in the transient dynamic simulation

when using the full FE model and a small time step [18].

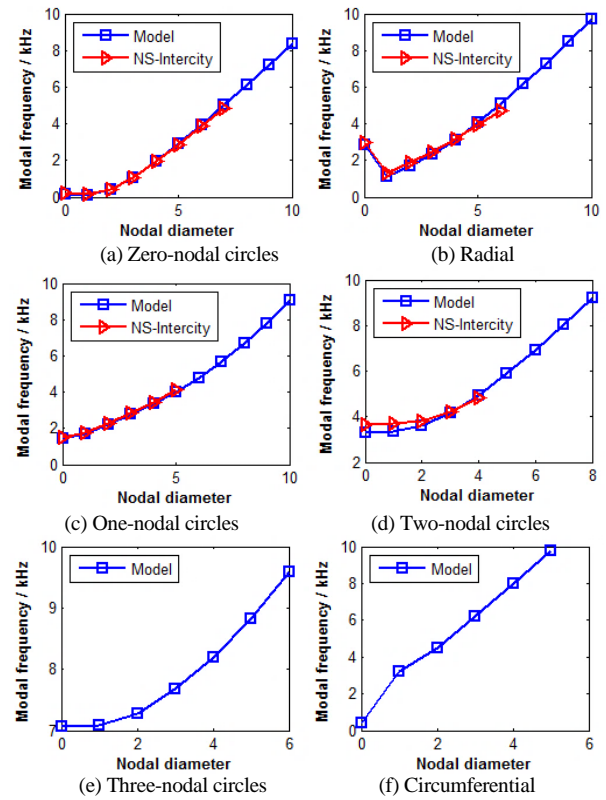


Fig. 2 Wheel modes calculated by a FE modal analysis (blue) compared with the measured results (red, from [23])

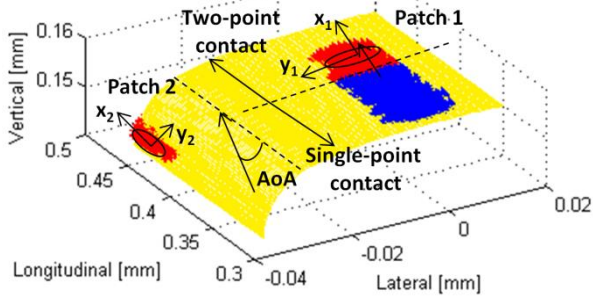
### 3. SOLUTION OF THE CONTACT MODEL

To study the dynamic transition from single-point to two-point contact, the contact positions between the wheel and rail must be identified first. Then, the time histories of the normal and tangential contact forces of the two contact points are calculated to present a load transmission during the contact transition. The emphasis of the contact solution is on the evolution of the distributions of the pressure, surface shear stress, adhesion-slip region and wheel-rail relative velocities in the contact patch. The solutions of 9 continuous time steps, 5 before and 4 during the occurrence of the two-point contact, are included in the analyses. The main purpose is to gain an insight into the dynamic effects during the wheel/rail contact transition.

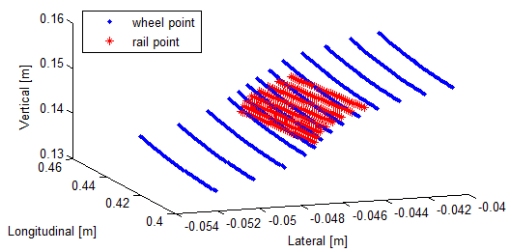
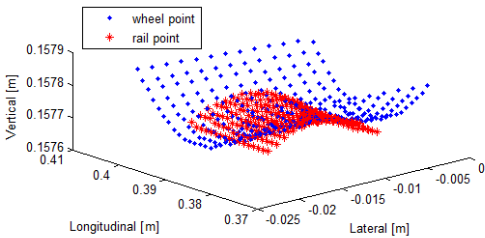
#### 3.1. Contact positions

The measurement indicates that the unstable vibration of the wheel (radiating squeal noise) is likely to occur when the AoA is between 15 and 25 mrad [30]. Three different AoAs—15, 20 and 25 mrad—are adopted in the simulations to emphasize the dynamic effects brought about by the unstable vibrating wheel. The simulated wheel-rail contact positions in the solution zone with AoA=20 mrad are presented in Fig. 3 (a). The yellow area represents the rail surface in the solution zone. The origin of the coordinate system is at the centre of the rail bottom surface at the initial

position of the wheel-rail contact. Hereafter, the coordinate system already includes the rail inclination in the track. By applying an explicit central difference time integration and a surface-to-surface contact-searching scheme based on a master-slave algorithm [19], the nodal forces in the solution zone in each time step can be calculated. The positions, shapes and areas of the contact patches are determined with the normal nodal force: a surface node is in contact if the normal nodal force is non-zero. Initially, the wheel-rail contact occurs only between the rail top and wheel tread. A trail of blue patches represents the ‘footprints’ of the single-point contact in a series of time steps. Due to the presence of an AoA, the wheel flange moves toward the gauge corner as the time step goes on and the 2<sup>nd</sup> contact patch starts to appear. The ‘footprints’ of the contact patches in the case of two-point contact are shown as two trails of red patches on the rail top and gauge corner. The coordinates of the wheel/rail nodes in and around the two oval-shaped contact patches (labelled as ‘Patch 1’ and ‘Patch 2’ in Fig. 3 (a)) from the same time step are plotted in Fig. 3 (b). The contact angle within the range of ‘Patch 2’ is between approximately 65° and 75°. The local lateral and longitudinal directions of Patches 1 and 2 on the rail surface are denoted by vectors  $x_1$  and  $y_1$  and vectors  $x_2$  and  $y_2$ , respectively, as shown in Fig. 3 (a).



(a) Contact patch ‘footprints’ on the rail (Blue for single-point contact and red for two-point contact)



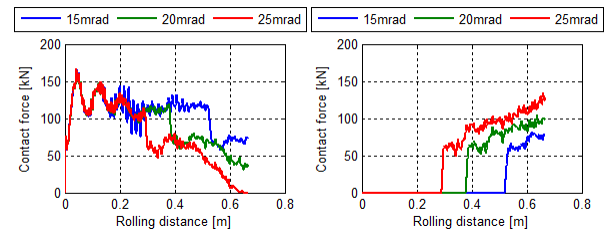
(b) Coordinates of nodes in/around two-point contact patches. (Upper figure: wheel tread-rail crown contact; Lower figure: flange-gage corner contact)

Fig. 3. Contact patches in the solution zone

### 3.2. Contact forces

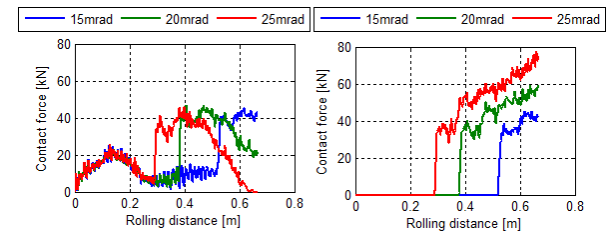
The time histories of the normal load and the lateral and longitudinal creep forces at the two contact patches are plotted in Fig. 4 with different AoAs. With the same initial wheel-rail clearance and train speed, a larger AoA leads to a larger lateral speed and consequently an earlier occurrence of the two-point contact. This can be identified according to the positions of the sudden jumps and drops of the curves in Fig. 4. The earliest two-point contact occurs at 0.29 m, when AoA=25 mrad. A non-steady-state feature (inconstant statistical properties along the time history) of the contact forces can be observed during the contact transition.

The oscillations of the curves before 0.29 m in Fig. 4 (a), (c) and (e) are due to vibrations excited by the initial kinetic and potential energy in the unbalanced system. Because the oscillations are damped out to less than 10% of the static values at 0.29 m, they have only a slight influence on the contact solutions presented in the following sections. The wheel-rail rolling always physically excites vibrations of the structure and waves in the continua. Thus, the real-world quantities fluctuate around their equilibrium values. When flange contact arises, the normal load and longitudinal creep force of Patch 1 in Fig. 4 (a) and (e) decrease, whereas those of Patch 2 in Fig. 4 (b) and (f) increase, indicating that they are transmitted from Patch 1 to Patch 2. The time histories of the lateral creep forces follow a different trend; specifically, they jump at both contact patches, as shown in Figs. 4 (c) and (d).



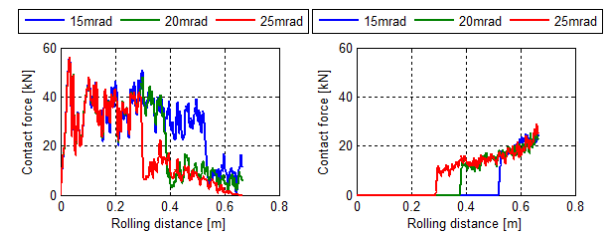
(a) Normal load of Patch 1

(b) Normal load of Patch 2



(c) Lateral force of Patch 1

(d) Lateral force of Patch 2



(e) Longitudinal force of Patch 1

(f) Longitudinal force of Patch 2

Fig. 4. Time history of the wheel-rail contact force

It can be expected that under the prescribed boundary condition shown in Fig. 1 (c), the wheel will tend to climb up on the rail when flange contact occurs. In this process, the contact forces of Patch 2 in all 3 directions will continue to increase, whereas those of Patch 1 will gradually decrease to zero. Then, the wheel tread will lose contact with the rail top, and all contact loads will be supported by Patch 2. This entire process is reproduced by the simulation with AoA=25 mrad. The simulated rolling distance in all 3 cases is sufficient to cover the transition from single-point to two-point contact.

In reality, the non-steady-state transition may last for a given period of time and then become (quasi-) steady at a certain moment when the transient effects decay. This phenomenon leads to research questions that should be addressed in future studies. For example, future studies should consider investigating the boundary conditions under which and at which moment a (quasi-) steady state can be achieved and to what extent the frictional rolling contact may affect this process.

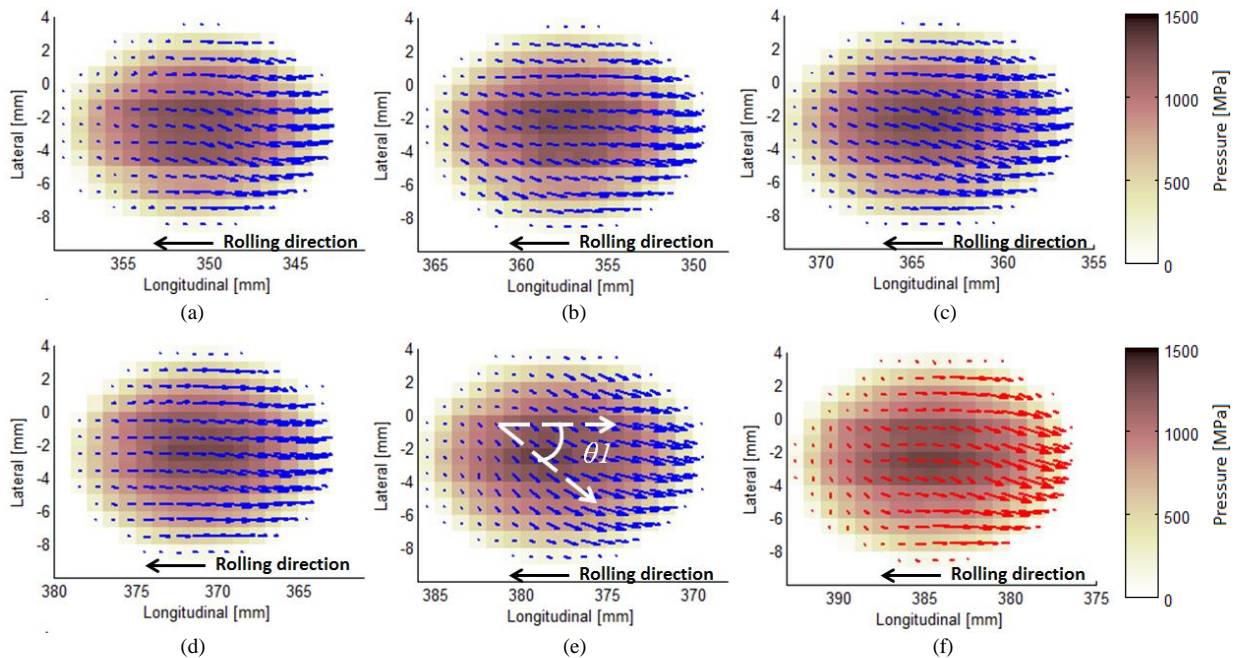
As shown in Fig. 4, the main trends of the simulated contact forces with different AoAs are similar. This is also true for the contact solutions analysed in the following sections. Therefore, only the results with AoA=20 mrad will be presented unless additional information can be provided by other simulations.

### 3.3. Pressure and surface shear stress

Stress analyses are crucial for understanding and predicting wheel/rail damage, such as wear and RCF [31]. The evolution of the contact pressure, together with the direction and magnitude of the surface shear

stress, are plotted in the contour/vector diagrams in Figs. 5 and 6 for Patches 1 and 2, respectively. The pressure magnitude corresponds to the depth of colour within the contact patch, as indicated by the colour bar. It shows that the size of Patch 1 shrinks and the size of Patch 2 expands once it has arisen at (f). Fig. 6 (i) only shows a part of Patch 2; the other part is out of the solution zone, i.e., beyond 0.45 m. Due to the existence of the AoA, the symmetrical axes of Patch 2 (if they exist) are not parallel to the lateral and longitudinal axes of the coordinate system, as in the case of Patch 1; in addition, the centres of Patches 1 and 2 from the same time step are not aligned along the lateral direction, as indicated in [24]. The maximum pressures of both patches are approximately in the middle of the respective patches.

The surface shear stresses in single-point and two-point contact are indicated by blue and red arrows, respectively. The arrows point in the direction of the shear stress, and their lengths are proportional to the magnitudes. To characterize the direction of the surface shear stress, the orientation angle between the stress vector and the negative direction of the longitudinal axis is denoted as  $\theta 1$  and  $\theta 2$  in Patches 1 and 2, respectively, as labelled in Figs. 5 (e) and 6 (f).  $\theta 1$  is typically small under a single-point contact (Fig. 5 (a)-(e)), but it increases rapidly to approximately  $90^\circ$  under two-point contact (Fig. 5 (f) - (i)) and as the participation of the 2<sup>nd</sup> contact patch increases (Fig. 6 (f) - (i)).  $\theta 1$  decreases from the leading part to nearly zero in the trailing part, when single-point contact occurs; this gradual change in  $\theta 1$  is likely caused by the geometry spin near the flange root in combination with the AoA with which the wheel negotiates a curve. Fig. 6 illustrates that  $\theta 2$  changes only slightly from the first occurrence of Patch 2 onward.



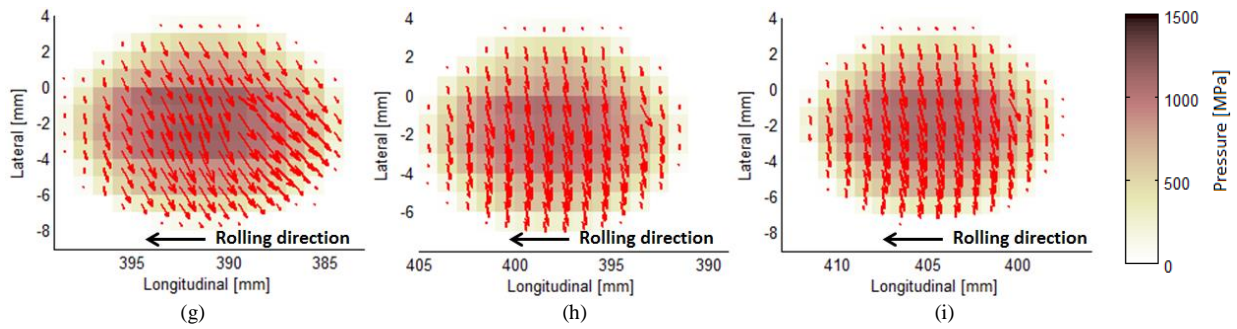


Fig. 5. Evolution of pressure and surface shear stress distributions in Patch 1 (Blue colour for shear stress indicates single-point contact; red indicates two-point contact)

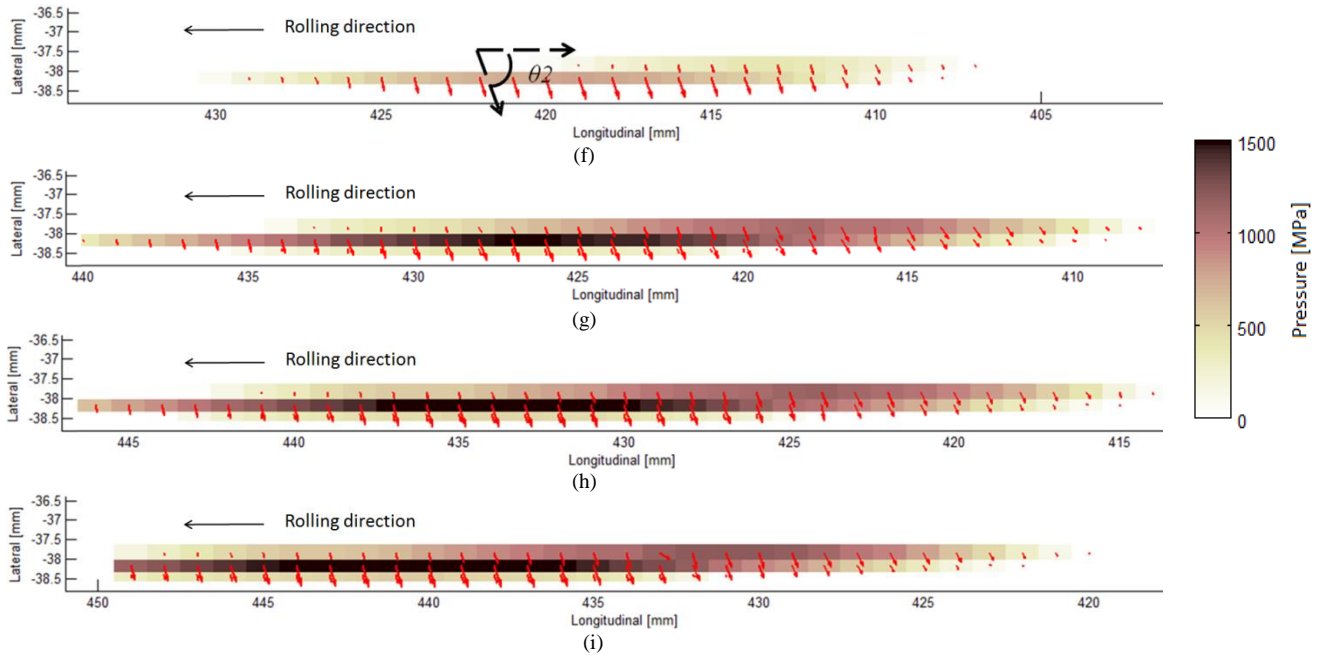


Fig. 6. Evolution of pressure and surface shear stress distributions in Patch 2 (Red colour for shear stress indicates two-point contact)

The change in the directions of the surface shear stress when two-point contact occurs results from the changes in the magnitude of the stresses in the lateral and longitudinal directions. The specific changes in the magnitude of the surface shear stress in the lateral and longitudinal directions, as well as  $\theta_1$  and  $\theta_2$ , are presented in Fig. 7 for 3 different AoAs. The values adopted here are the average of all elements within the contact patch. The abscissa of the figures is the serial number of the contact patch in the evolution (from a series of time steps), with an interval of 6.7 mm. For all three AoA values, the lateral shear stress (upper row of Fig. 7) increases dramatically when Patch 2 arises, and the lateral shear stress of Patch 2 is larger than that of Patch 1. As shown by Figs. 4 (c) and (d), the lateral creep forces at the two contact patches are similar in the early period of the transition (within 0.1 m after the jumps of the curves), whereas the lateral shear stress of Patch 2 is larger because of its smaller size. In the middle row of Fig. 7, the longitudinal shear stress of Patch 1 declines to a certain extent because of the participation of Patch 2. The bottom row shows that the absolute value of  $\theta_1$  stays in the range of less than  $20^\circ$  in the stage of single-point contact, jumping to

approximately  $70^\circ$  in 2-3 output time steps once Patch 2 appears.  $\theta_2$  is always between  $60^\circ$  and  $70^\circ$ . This narrow range of high values may be related to the initiation and growth of head checks, whose orientation is also typically within a narrow range of angles, and their developments are approximately perpendicular to the direction of the surface shear stress (or tangential force) [32]. In addition, the calculated large pressure (up to 1,500 MPa) and surface shear stress (up to 450 MPa) with a large orientation angle  $\theta_2$  at Patch 2 may lead to severe wear [33] and downward plastic flow at the rail gauge corner [6]. A typical rail sample with severe wear and downward plastic flow at the gauge corner can be found in Fig. 8.

A comparison of the shear stresses under different AoAs in Fig. 7 illustrates that with increases in the AoA, the lateral shear stress of Patch 2 increases but the longitudinal shear stress decreases, causing an increase in  $\theta_2$ . For Patch 1, the longitudinal shear stress is slightly raised by applying a larger AoA, as shown in the middle row of Fig. 7, because a smaller longitudinal load is transmitted to Patch 2 (compare Figs. 4 (e) and (f)). This comparison must be made at

the incipient moment of the two-point contact, that is, the curves in Figs. 4 (e) and (f) should be shifted such

that the jumps of the curves between 0.2 and 0.6 m coincide to render the difference at the jump visible.

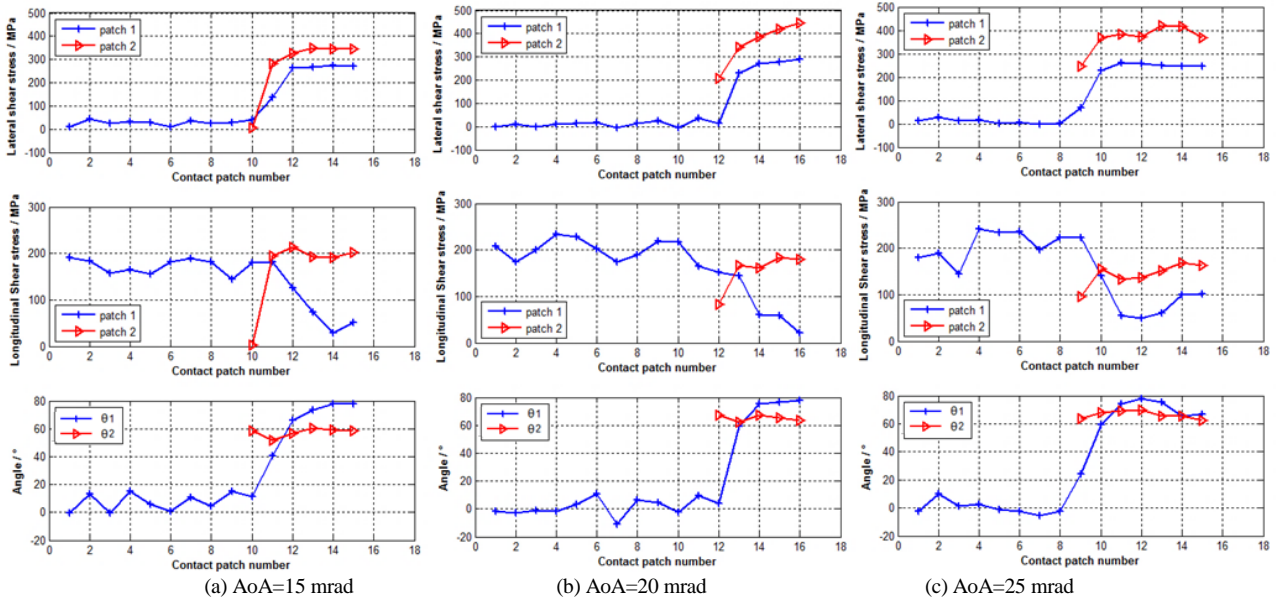


Fig. 7. Changes in the surface shear stresses and orientation angles with different AoAs (upper graphs: lateral stress; middle graphs: longitudinal stress; bottom graphs: orientation angle)



Fig. 8. severe wear and downward plastic flow at the rail gauge corner

### 3.4. Adhesion-slip distribution

The division of the adhesion and slip regions in the contact patch is an important feature of the frictional rolling contact. It can be derived by comparing the value  $F_n \times f - F_t$  with a tolerance  $\varepsilon_T$ , where  $F_n$ ,  $F_t$  and  $f$  are the pressure, surface shear stress, and friction coefficient, respectively, and  $\varepsilon_T$  is set as a percentage of the largest tangential nodal force in the contact patch, as in [18]. The pressure and surface shear stresses plotted in Figs. 9 and 10, respectively, under single-point and two-point contact conditions are extracted from the stress distribution graphs in Figs. 5 and 6 along the longitudinal centre lines of the contact patches.

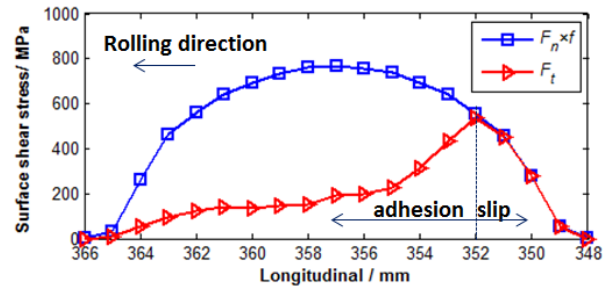


Fig. 9. Stress distribution along the longitudinal axis under single-point contact

Because the stress and adhesion-slip area distributions in single-point contact have been well studied in the literature [18,19], only the results of one time-step (extracted from Fig. 5 (b)) are presented in Fig. 9. These results correspond well with the results in [18,19].

The adhesion-slip area distributions in Figs. 10 (a), (b), (c) and (d) for two-point contact correspond to the stress distributions in Figs. 5 (f), (g), (h) and (i), respectively. The left-hand side graph of Fig. 10 (a) is similar to that of single-point contact in Fig. 9. With the progression of the transition, the adhesion area in Patch 1, indicated by the gaps between the two curves, is reduced in Fig. 10 (b) and has completely vanished in Figs. 10 (c) and (d).

The right-hand side graphs of Fig. 10 (a) show that when the 2<sup>nd</sup> patch has just come into being, its size is small and its pressure and surface shear stress are low compared to those in Figs. 10 (b), (c) and (d). For the same reason as in Fig. 6 (i), only a part of Patch 2 is included in Fig. 10 (d). The graphs also show that

Patch 2 is fully in slip so far, namely,  $F_n \times f = F_t$ , according to the Coulomb's law employed in the model.

Figs. 10 (c) and (d) illustrate that due to the two-point contact, the entire contact area, including Patches 1 and

2, evolves into complete slip. This may further lead to unstable stick-slip rolling, an important cause of 'rutting' (a specific type of short-pitch corrugation in curves) [34] and curve squeal noise [23].

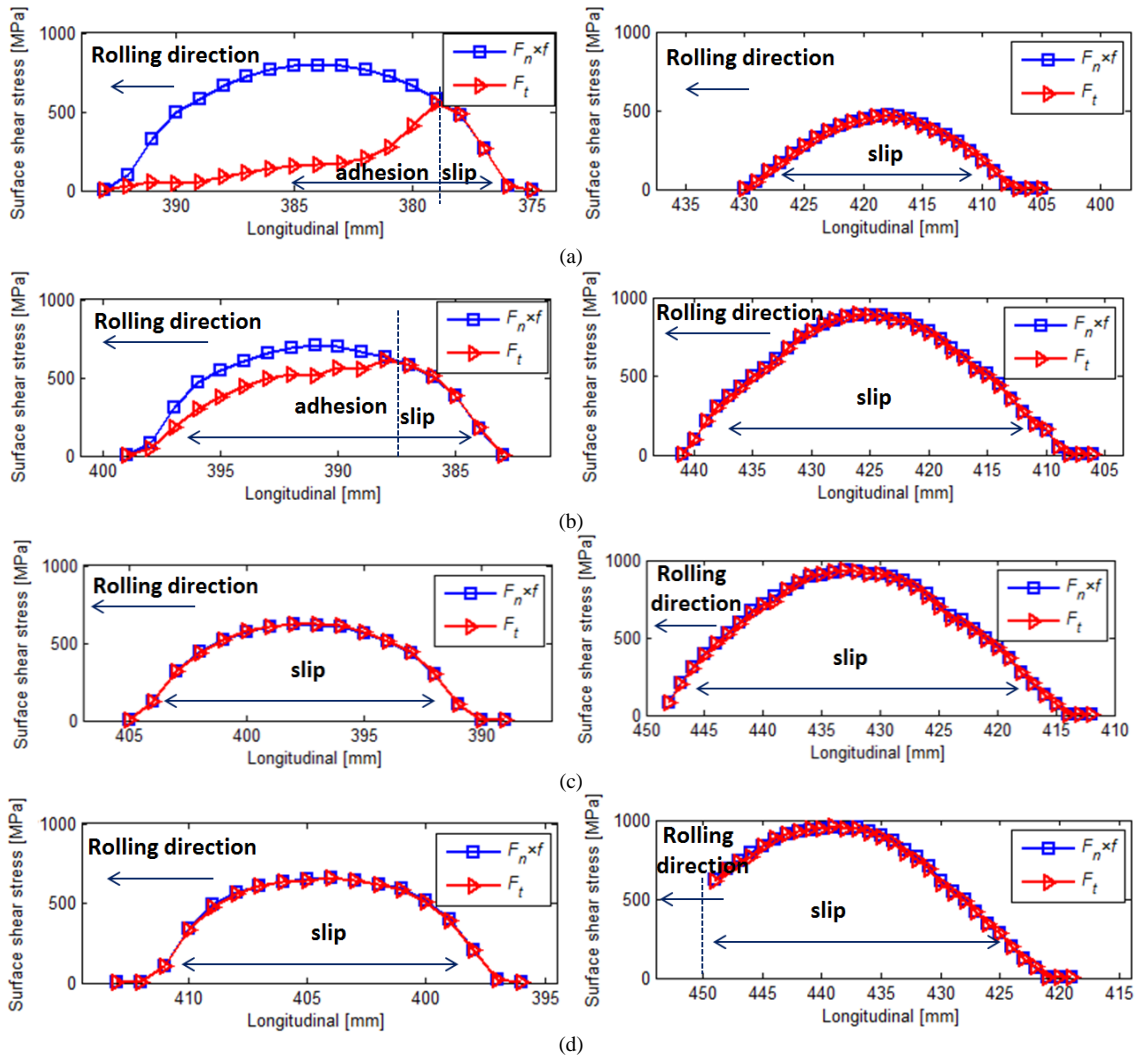


Fig. 10. Stress distribution along the longitudinal axis under two-point contact condition (left-hand side graphs: Patch 1; right-hand side graphs: Patch 2)

### 3.5. Wheel-rail relative velocity

The analyses of the wheel-rail relative velocities in the contact patch are distinguished in the normal and tangential directions. The evolutions of the distributions of the wheel-rail relative velocities in both directions are combined in the contour/vector diagrams in Figs. 11 and 12 for Patches 1 and 2, respectively.

#### 3.5.1 Micro-slip

The tangential wheel-rail relative velocity, the so-called micro-slip, refers to the relative velocity between two contact particles. The adhesion-slip area distribution can also be derived from the micro-slip analysis. The contact and adhesion regions of Patch 1 are indicated by black ovals in Fig. 11. The adhesion-slip distributions shown here are in line with the results obtained by the stress analyses in Figs. 9 and 10.

Similar to the stress distribution shown in Figs. 5 and 6, the micro-slips under single-point and two-point contact conditions are also indicated by blue and red arrows, respectively. The arrows point in the directions of the micro-slip, and their lengths are proportional to the magnitudes. A comparison of the micro-slip graphs with the surface shear stress graphs illustrates that the general direction of the micro-slip is opposite to and changes together with the direction of the surface shear stress: as the transition proceeds, the direction of the micro-slip in Patch 1 changes from in the longitudinal direction ( $\theta \approx 0^\circ$ ) to in the lateral direction ( $\theta \approx 90^\circ$ ), whereas the change in direction for the Patch 2 micro-slip is less pronounced.

#### 3.5.2 Normal relative velocity

The magnitude of the normal relative velocity is indicated by the colour depth within the contact patches in Figs. 11 and 12 for single-point and two-point contact, respectively. The colour outside the contact patch corresponds to a zero relative velocity, whereas a positive (lighter colour) or negative (darker

colour) relative velocity corresponds to the condition that the wheel and rail surface elements move toward or away from each other, respectively. The colours at the leading and trailing edges of the contact patch are lighter and darker, respectively.

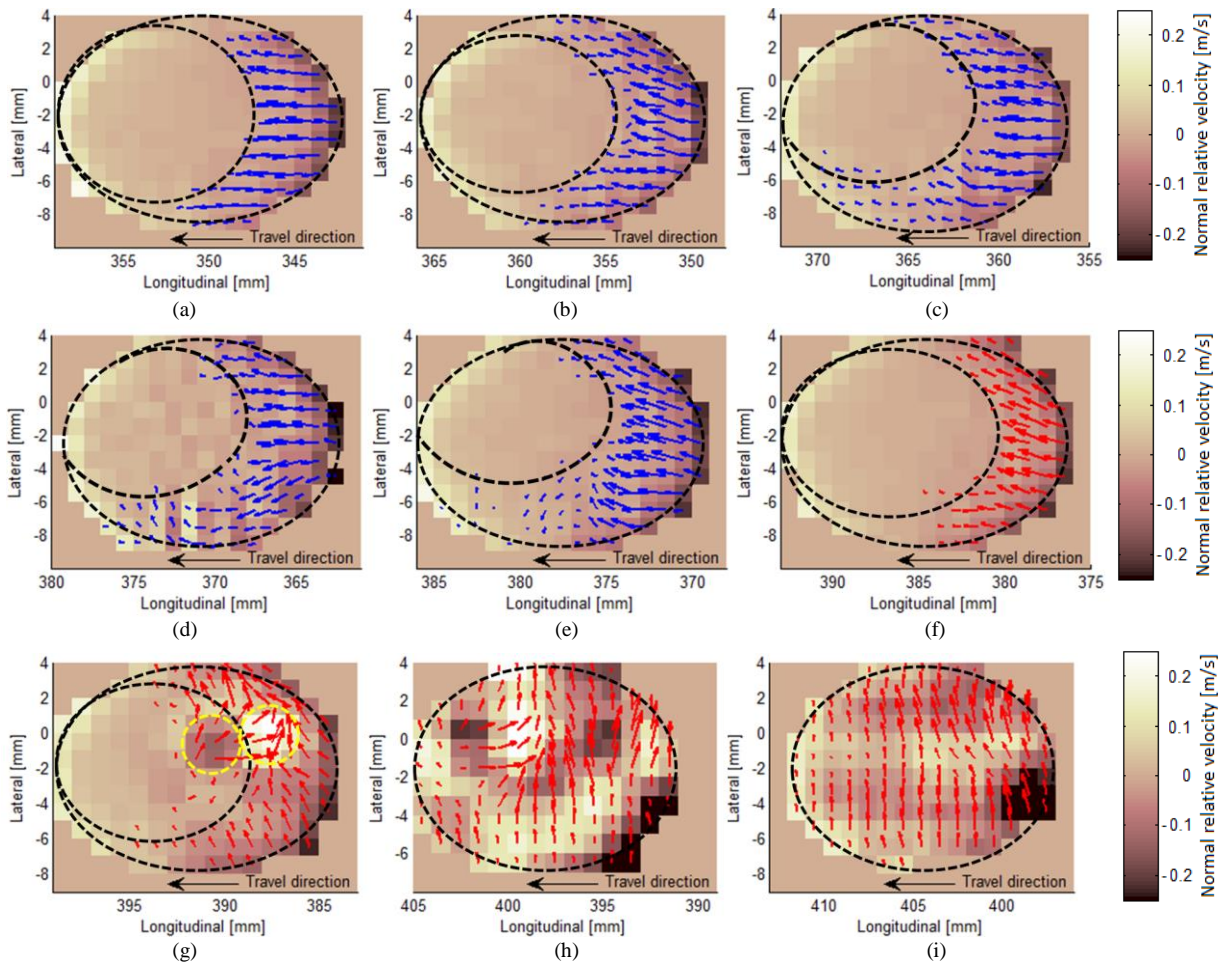


Fig. 11. Evolution of the distribution of the wheel-rail relative velocity in Patch 1

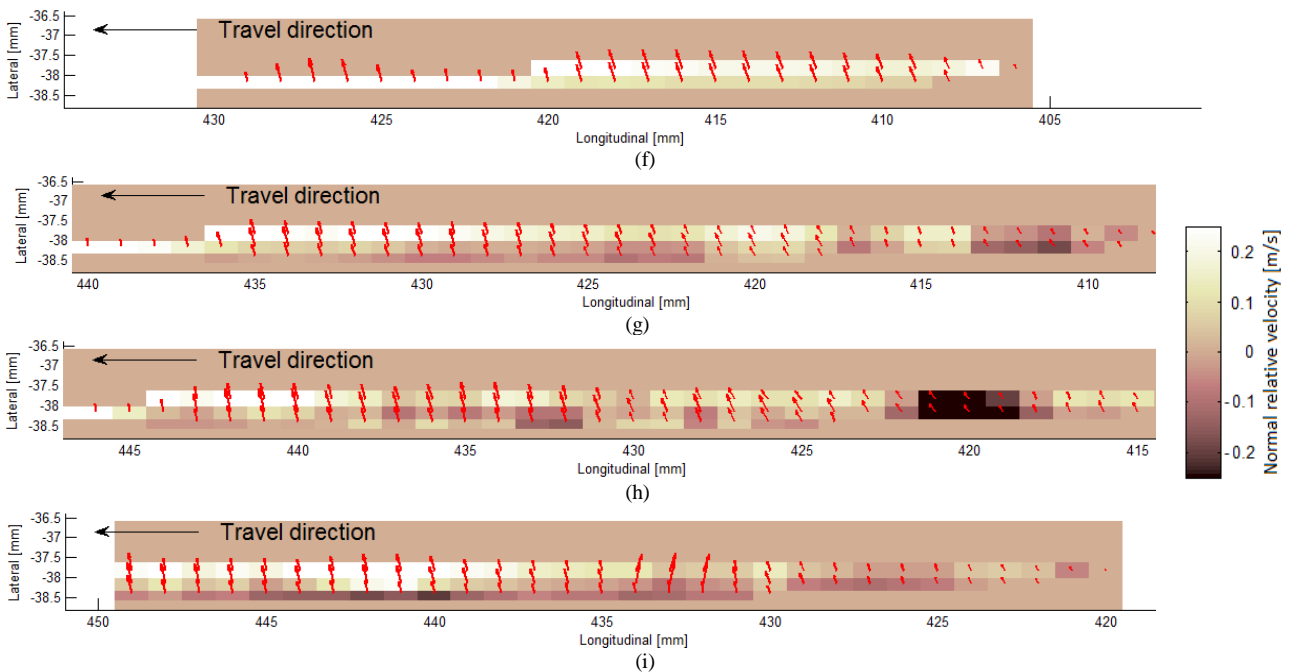


Fig. 12. Evolution of the distribution of the wheel-rail relative velocity in Patch 2

### 3.5.3 Local intensification and relaxation of compression

Because the surface elements of the wheel and rail are in contact, the further movement toward or away from each other will cause the transient intensification or relaxation of the contact, respectively. Therefore, the lighter or darker areas within the contact patches in Figs. 11 and 12 reflect the transient local compression intensification or relaxation, respectively.

### 3.5.4 Contact turbulence and waves

Figs. 11 and 12 illustrate the influence of the transient dynamics on the wheel-rail contact. Such local dynamics, coming from the wheel-rail vibrations and wave propagation, is less visible in the stress analyses of Figs. 5 and 6 because the vibrating displacements in the contact patch are not sufficiently large to cause a clear stress turbulence, although they do affect the stress distribution, as reported in [18]. As the first-order derivative of the displacement, the vibrating velocity is more sensitive to the dynamic turbulence.

Comparing Figs. 11 (f) and (g) illustrates that under the two-point contact condition, a turbulence of micro-slip, i.e., the chaotic direction of the micro-slip, is likely to be initiated next to the juncture of the adhesion and slip regions, where the maximum surface shear stress is located, as shown in the yellow ovals in Fig. 11 (g). Moreover, this tangential turbulence arises together with the transient local compression intensification and relaxation at the same location of contact patch, indicated by the lighter and darker spots, respectively, in the yellow ovals.

Figs. 11 (a) to (e) for the single-point contact illustrate that a turbulence of an (irregular) micro-slip distribution appears to start at the leading bottom part of the contact patch and propagate upward and toward the trailing direction. The expansion of this turbulence, together with the increasing geometrical spin when approaching flange contact, causes the adhesion region to move upward in the contact patch.

Compared to the single-point contact condition, a more obvious local compression intensification and relaxation is observed in the two-point contact condition.

Embodied in the alternation of the compression intensification and relaxation, an intensification-relaxation wave can be observed within the contact patch. The wave appears to propagate radially, as shown in Fig. 11 (h), or parallel to the micro-slip vectors, as shown in Fig. 13, calculated for the case of  $AoA=25$  mrad. According to the vibration frequencies of the surface nodes and the wavelengths observed in Fig. 11 (h) and Fig. 13, the wave propagating speed can be estimated as about 3 km/s, falling within the range of Rayleigh wave. Moreover, the phase

difference between normal and tangential surface nodal vibrations is approximate  $\pi/2$ , corresponding well with the feature of Rayleigh wave.

As shown in Figs. 11 (d), (g), (h) and (i), as well as in Fig. 13, the turbulence of the micro-slip always comes together with the transient local compression intensification and relaxation at the same location. Moreover, the micro-slips in the relaxation areas are normally larger than those in the adjacent intensification areas. This inhomogeneous distribution of reciprocating motion within the wheel-rail contact could cause fretting.

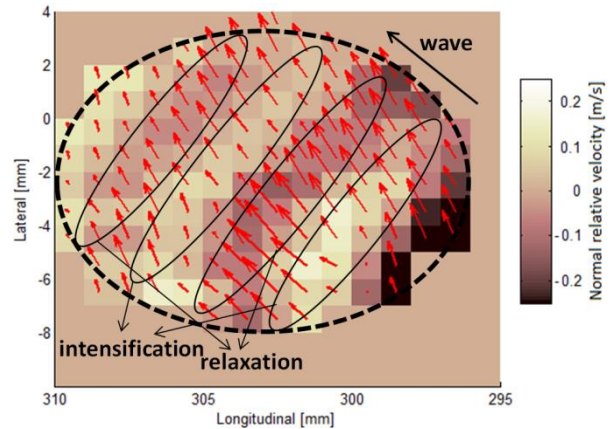


Fig. 13. Distribution of wheel-rail relative velocity in Patch 1 under two-point contact condition with  $AoA=25$  mrad

The compression intensification and relaxation can also be observed in Patch 2 in Fig. 12, but the patterns are comparatively less regular. In addition, in Fig. 12 (i), the micro-slip direction at the position 432-434 mm along the longitudinal axis appears abnormal. Correspondingly, the direction of the surface shear stress, shown in Fig. 6 (i), at the same position is also notably different from the others. As suggested in [18], an element size of 1/10 of the minor axis or smaller should be used with the FEM in engineering applications. Future studies should investigate whether the irregular wave pattern and the deviated micro-slip are greater due to the coarse element size in relation to the narrow contact patch or physically exist due to the slip turbulence and the compression intensification and relaxation.

## 4. CONCLUSIONS AND FUTURE WORK

This paper simulates non-steady-state rolling contact with a transition from single-point to two-point contact by an explicit FEM. The structural dynamics of the wheel-track system is coupled with the continuum dynamics of frictional rolling. The wheel model is validated against measurement results from the literature. The stress and adhesion-slip distribution under the single-point contact condition and the positions and shapes of the contact patches under the two-point contact condition correspond well with the

results in the literature. The major findings of the study are as follows:

- Transient dynamic effects can be captured by the relative velocity in the wheel-rail contact.
- Wave propagation is excited in the wheel and rail continua, especially by the transition from single-point to two-point contact. The vibrations and waves may cause local compression intensification and relaxation of the contact, as well as local turbulence of the micro-slip.
- The compression intensification and relaxation and the micro-slip turbulence always occur simultaneously and at the same locations, and they are likely initiated next to the juncture of the adhesion and slip regions in the contact patch, where the maximum surface shear stress is located.
- The intensification-relaxation wave appears to propagate radially or parallel to the micro-slip vectors. The micro-slip in the relaxation area is larger than that in the adjacent intensification area. This phenomenon may cause fretting.
- Compared to those in single-point contact, stronger waves, the resulting micro-slip turbulence, and the transient local compression intensification and relaxation can be observed upon the occurrence of the 2<sup>nd</sup> contact point. Moreover, the contact transition can cause the full slip of the entire wheel-rail contact. These factors may contribute to contact instability and ultimately corrugation and squeal.

The method presented in this paper could enable the more realistic modelling of wheel-rail frictional rolling in the study of wear and rolling contact fatigue. In further studies, field and lab measurement of wheel-rail force during contact transition is going to be performed to confirm the results of load transition and friction saturation predicted by the numeric model. The wear, believed to be proportional to the frictional work [35], can be computed readily from the dynamic contact stress and micro-slip results obtained in this paper. The pressure and surface shear stress at the rail gauge corner calculated in this study are large, and the orientation angle is always at a high value between 60° and 70°. Whether these results are related to the initiation and growth of the head check can be further investigated by assessing the near-surface von Mises stress, ideally with a finer-meshed gauge corner model. Since wheel and rail profiles may influence contact solutions and wheel-rail dynamics, worn pair of wheel-rail surfaces should be considered in future study by applying the approach presented in this paper.

The intensification and relaxation may reflect some of the important wheel-rail dynamic characteristics, whereas the irregular micro-slip mirrors the frictional contact turbulence. Thus, the calculated wheel-rail

relative velocities appear to connect the wheel-rail dynamic properties to the frictional rolling contact, plausibly providing a more physical and sensitive method than those relying on the steady-state contact force calculation. Based on the method presented in this paper, the generation mechanism of the 'erratic' squeal noise generation and the 'elusive' corrugation could be studied in the future.

## 5. REFERENCES

- [1] Piotrowski J, Kik W. A simplified model of wheel/rail contact mechanics for non-Hertzian problems and its application in rail vehicle dynamic simulations. *Vehicle System Dynamics* 2008; 46: 27-48. doi: 10.1080/00423110701586444.
- [2] Ayasse JB, Chollet H. Determination of the wheel rail contact patch for semi-Hertzian conditions. *Vehicle System Dynamics* 2005; 43: 161-72. doi: 10.1080/00423110412331327193.
- [3] Kalker JJ. *Three dimensional elastic bodies in rolling contact*. Dordrecht: Kluwer Academic Publisher; 1993. doi: 10.1115/1.2900773.
- [4] Sichani MS, Enbloma R, Berg M. A novel method to model wheel-rail normal contact in vehicle dynamics simulation. *Vehicle System Dynamics* 2014; 52: 1752-64. doi: 10.1080/00423114.2014.961932.
- [5] Sichani MS, Enbloma R, Berg M. An alternative to FASTSIM for tangential solution of the wheel-rail contact. *Vehicle System Dynamics* 2016; doi: 10.1080/00423114.2016.1156135.
- [6] Li Z. *Wheel-rail rolling contact and its application to wear simulation (Doctoral Thesis)*. Delft University of Technology; 2002.
- [7] Burgelman N, Li Z, Dollevoet R. A new rolling contact method applied to conformal contact and the train–turnout interaction. *Wear* 2014;321:94-105. doi: 10.1016/j.wear.2014.10.008.
- [8] Yan W, Fischer FD. Applicability of the hertz contact theory to rail-wheel contact problems. *Arch Appl Mech* 2000;70:255-68. doi: 10.1007/s004199900035.
- [9] Ringsberg JW, Josefson BL. Finite element analyses of rolling contact fatigue crack initiation in railheads. *Proceedings of the Institution of Mechanical Engineers, Part F: Journal of Rail and Rapid Transit* 2001;215:243-59.
- [10] Telliskivi T, Olofsson U. Wheel–rail wear simulation. *Wear* 2004;257:1145-53. doi: 10.1016/j.wear.2004.07.017.
- [11] Sladkowski A, Sitarz M. Analysis of wheel–rail interaction using FE software. *Wear* 2005;258:1217-23. doi: 10.1016/j.wear.2004.03.032.

- [12] Magheri S, Malvezzi M, Meli E, Rindi A. An innovative wheel-rail contact model for multibody applications. *Wear* 2011; 271: 462-71. doi: 10.1016/j.wear.2010.10.038.
- [13] Meli E, Magheri S, Malvezzi M. Development and implementation of a differential elastic wheel-rail contact model for multibody applications. *Vehicle System Dynamics* 2011; 49: 969-1001. doi: 10.1080/00423114.2010.504854.
- [14] Wen Z, Jin X, Zhang W. Contact-impact stress analysis of rail joint region using the dynamic finite element method. *Wear* 2005;258:1301-9. doi: 10.1016/j.wear.2004.03.040.
- [15] Li Z, Zhao X, Esveld C, Dollevoet R, Molodova M. An investigation into the causes of squats—Correlation analysis and numerical modeling. *Wear* 2008;265:1349-55. doi: 10.1016/j.wear.2008.02.037.
- [16] Wiest M, Daves W, Fischer FD, Ossberger H. Deformation and damage of a crossing nose due to wheel passages. *Wear* 2008;265:1431-8. doi: 10.1016/j.wear.2008.01.033.
- [17] Pletz M, Daves W, Ossberger H. A wheel set/crossing model regarding impact, sliding and deformation—explicit finite element approach. *Wear* 2012;294:446-56. doi: 10.1016/j.wear.2012.07.033.
- [18] Zhao X, Li Z. The solution of frictional wheel-rail rolling contact with a 3D transient finite element model: validation and error analysis. *Wear* 2011;271:444-52. doi: 10.1016/j.wear.2010.10.007.
- [19] Deng X, Qian Z, Dollevoet R. Lagrangian explicit finite element modeling for spin-rolling contact. *J Tribol* 2015;137:041401. doi: 10.1115/1.4030709.
- [20] Wriggers P. *Computational contact mechanics*. 2nd ed. Berlin: Springer Verlag; 2006.
- [21] Mulvihill DM, Kartal ME, Nowell D, Hills DA. An elastic-plastic asperity interaction model for sliding friction. *Tribol Int* 2011;44:1679-94 doi: 10.1016/j.triboint.2011.06.018.
- [22] Chen GX, Zhou ZR, Ouyang H, Jin XS, Zhu MH, Liu QY. A finite element study on rail corrugation based on saturated creep force-induced self-excited vibration of a wheelset-track system. *J Sound Vib* 2010;329:4643-55. doi: 10.1016/j.jsv.2010.05.011.
- [23] Thompson DJ. *Railway noise and vibration: mechanisms, modelling and means of control*. Amsterdam: Elsevier; 2009.
- [24] Vo KD, Zhu HT, Tieu AK, Kosasih PB. FE method to predict damage formation on curved track for various worn status of wheel/rail profiles. *Wear* 2015;322:61-75. doi: 10.1016/j.wear.2014.10.015.
- [25] Chongyi C, Chengguo W, Ying J. Study on numerical method to predict wheel/rail profile evolution due to wear. *Wear* 2010;269:167-73. doi: 10.1016/j.wear.2009.12.031.
- [26] Wei Z, Li Z, Qian Z, Chen R, Dollevoet R. 3D FE modelling and validation of frictional contact with partial slip in compression-shift-rolling evolution. *International Journal of Rail Transportation* 2015; 4: 20-36. doi: 10.1080/23248378.2015.1094753.
- [27] Zhao X, Li Z, Liu J. 2012. Wheel-rail impact and the dynamic forces at discrete supports of rails in the presence of singular rail surface defects. *Proceedings of the Institution of Mechanical Engineers, Part F: Journal of Rail and Rapid Transit* 2001;226:124-39. doi: 10.1177/0954409711413975.
- [28] Courant R, Friedrichs K, Lewy H. On the partial difference equations of mathematical physics. *IBM J Res & Dev* 1967;11:215-34. doi: 10.1147/rd.112.0215.
- [29] Glocker C, Cataldi-Spinola E, Leine RI. Curve squealing of trains: measurement, modelling and simulation. *J Sound Vib* 2009;324:365-86. doi: 10.1016/j.jsv.2009.01.048.
- [30] Anderson D, Wheatley N, Fogarty B, Jiang J, Howie A, Potter W. Mitigation of curve squeal noise in Queensland, New South Wales and South Australia. In: *Conference on Railway Engineering*. Perth, Australia: Railway Technical Society of Australasia; 2008, p. 625-36.
- [31] Zerbst U, Lundén R, Edel KO, Smith RA. Introduction to the damage tolerance behaviour of railway rails—a review. *Eng Fract Mech* 2009;76:2563-601. doi: 10.1016/j.engfracmech.2009.09.003.
- [32] He CG, Huang YB, Ma L, Guo J, Wang WJ, Liu QY, et al. Experimental investigation on the effect of tangential force on wear and rolling contact fatigue behaviors of wheel material. *Tribol Int* 2015;92:307-16. doi: 10.1016/j.triboint.2015.07.012.
- [33] Sundh J, Olofsson U. Seizure mechanisms of wheel-rail contacts under lubricated conditions using a transient ball-on-disc test method. *Tribol Int* 2008;41:867-74. doi: 10.1016/j.triboint.2007.12.011.
- [34] Grassie SL. 2009. Rail corrugation: characteristics, causes, and treatments. *Proceedings of the Institution of Mechanical Engineers, Part F: Journal of Rail and Rapid Transit* 2009;223:1-16. doi: 10.1243/09544097JRRT264
- [35] Archard JF. Contact and rubbing of flat surfaces. *J Appl Phys* 1953;24:981-8. doi: 10.1063/1.1721448.